Influence of Alloy Content and Prior Microstructure on Evolution of Secondary Phases in Weldments of 9Cr-Reduced Activation Ferritic-Martensitic Steel

V. THOMAS PAUL, C. SUDHA, and S. SAROJA

9Cr-Reduced Activation Ferritic-Martensitic steels with 1 and 1.4 wt pct tungsten are materials of choice for the test blanket module in fusion reactors. The steels possess a tempered martensite microstructure with a decoration of inter- and intra-lath carbides, which undergoes extensive modification on application of heat. The change in substructure and precipitation behavior on welding and subsequent thermal exposure has been studied using both experimental and computational techniques. Changes *i.e.*, formation of various phases, their volume fraction, size, and morphology in different regions of the weldment due to prolonged thermal exposure was influenced not only by the time and temperature of exposure but also the prior microstructure. Laves phase of type Fe_2W was formed in the high tungsten steel, on aging the weldment at 823 K (550 °C). It formed in the fine-grained heat-affected zone (HAZ) at much shorter durations than in the base metal. The accelerated kinetics has been understood in terms of enhanced precipitation of carbides at lath/grain boundaries during aging and the concomitant depletion of carbon and chromium and enrichment of tungsten in the vicinity of the carbides. Therefore, the fine-grained HAZ in the weldment was identified as a region susceptible for failure during service.

I. INTRODUCTION

HIGH chromium (9 to 12 pct) ferritic/martensitic steels with good thermal conductivity and superior void swelling resistance find application as core structural materials in nuclear fission reactors. The Cr-Mo steels are not suitable for service in high energy-high flux neutron environment, as encountered in nuclear fusion reactors due to the induced radioactivity of constituent elements like Mo and Nb.[1] Hence, a new variant of this class of steel the 'reduced activation' ferritic/martensitic steel (RAFM) was developed by (1) substituting W for Mo and Ta for Nb and (2) minimizing the other radio active elements, keeping its mechanical/thermal properties unaltered.[2–4] 9Cr-RAFM steel with good mechanical property, weldability, adequate creep strength [up to 873 K (600 °C)], and limited radiological activation in addition to better void swelling resistance was chosen for fabrication of Test Blanket Modules (TBM) in the International Thermo-nuclear Experimental Reactor.[5,6]

Development of RAFM steels have focused on tailoring the alloy chemistry, especially W and Ta contents to achieve satisfactory mechanical properties and weldability.[7,8] These and similar efforts led to enhanced understanding on the effect of varying W and Ta concentrations on creep rupture strength,[9,10] prior austenite grain (PAG) size refinement,[11] evolution and coarsening of precipitates,[12–14] and weldability.[15] Since welding is an inevitable fabrication process, study on structural and mechanical properties of the welded joints of 9Cr-RAFM steels is considered as a thrust area of research.[16–19]

For fabrication of TBM components, fusion welding techniques like electron beam welding, tungsten inert gas (TIG) welding, and laser beam welding are chosen where the extent of heat-affected zone (HAZ) is minimum compared to other conventional methods.[20] However, in fusion welding, the weldment would possess a highly heterogeneous microstructure depending on the distance of a region from the heat source and number of passes employed.[21,22] Since it is the microstructure that decides the response of a weldment to stresses subsequent to post-weld heat treatment or during long-term service exposures[23,24] many experimental studies focused on the change in structure and property of weld and HAZ upon varying the heat input and cooling rates during welding.[25,26]

Recently, genetic algorithm-based computation was attempted for optimizing the chemistry of RAFM steels in order to achieve desired volume fraction and coarsening rate of $M_{23}C_6$ carbides and Laves phase.[27] To perform such complex calculations or use

V. THOMAS PAUL, Scientific Officer E, is with the Material Synthesis and Structural Characterisation Division, Physical Metallurgy Group, Indira Gandhi Centre for Atomic Research, Kalpakkam, 603102, Tamil Nadu India. C. SUDHA, Scientific Officer F, and S. SAROJA, Head, are with the Microscopy and Thermo-physical Properties Division, Physical Metallurgy Group, Indira Gandhi Centre for Atomic Research. Contact e-mail: sudha_diwa@yahoo.co.in
Manuscript submitted November 10, 2014.
Article published online May 19, 2015.

CALPHAD-based thermodynamic approaches for multicomponent systems,[28,29] there is a prerequisite for the user to be familiar with the software structure, its individual modules, and commands. A Java-based software for modeling materials properties and behavior, 'JMatPro'[30] is available which is extremely user friendly and helpful to get information about stable phase equilibria and phase transformation. Klueh[31] used JMatPro to study the effect of boron addition in NF616 (9Cr-1.8W) steel, predict the amount of laves and precipitate phases in 9Cr-1WVTa and 9Cr-2WVTa steels, and also to propose the composition for improved versions of RAFM steels.

As a part of the long-term R&D efforts to support the fusion program in India, the India-Specific RAFM (INRAFM) steel with 1.4 wt pct W and 0.06 wt pct Ta was developed.[1] In the present study, weldments of INRAFM and 1W-RAFM (with 1W and 0.06Ta) steels were fabricated using TIG welding process. Microstructural evolution including coarsening of precipitates, change in microchemistry, and formation of laves phase in various regions of the weldments of INRAFM and 1W-RAFM steels after prolonged thermal exposures were studied using variety of experimental techniques. JMatPro was used to predict the formation of various phases and their volume fraction in different regions of the RAFM weldments. The predictions were validated by an extensive experimental characterization program. Comparison of the precipitation behavior of INRAFM and 1W-RAFM steels clearly demonstrated the role of W on the kinetics of Laves phase formation in different regions of the weldment.

II. EXPERIMENTAL DETAILS

12-mm-thick plates of RAFM steels with 1 and 1.4 wt pct W (hereafter 1W and INRAFM, respectively) were supplied in the normalized [1253 K (980 °C)] and tempered [1033 K (760 °C)] condition by M/s MIDHANI, Hyderabad, India. Chemical compositions of the steels are given in Table I. The plates were machined to 200 × 200 × 12 mm size and autogenous bead-on-plate weldments were fabricated by T1G welding to avoid (i) compositional changes in the weld metal and (ii) multiple thermal cycles. Welding parameters used in the present study are listed in Table II and schematic of the weld geometry is shown as Figure 1. Based on the microstructure, various regions of the weldment were identified as weld metal, HAZ1 (HAZ near to fusion line), HAZ2 (HAZ near to base metal), and base metal. Smaller 6-mm-wide specimens encompassing all the regions were extracted from the weldment for heat treatments. Specimens were aged in vacuum-sealed

quartz tubes at 773 K and 823 K (500 °C and 550 °C) for 5000 and 10,000 hours durations. Metallurgical investigations on 'as welded' (as received) and aged specimens were carried out on cross section samples prepared using standard metallographic practices.

Optical, scanning, and transmission electron microscopy (SEM and TEM), and hardness measurements were carried out on different regions of the weldment. Hardness profile across the weldment was obtained using 'Leitz miniload 2′ micro harness tester with an applied load of 100 g, whereas change in macro hardness value was monitored to assess the effect of thermal exposure. Philips XL30 ESEM operating at 30 kV was used for microstructural observations.

Analytical transmission electron microscope (Philips CM 200 ATEM) was used at an operating voltage of 120 to 200 kV to study both thin foil and carbon extraction replicas obtained from the weldment. Characteristic X-ray spectra acquired using INCA energy-dispersive spectrometer (EDS) were quantified using standard k_{AB} values. To prepare TEM specimens, specific regions of the weldment *i.e.*, weld metal, HAZ1, HAZ2, and base metal were sectioned separately parallel to the weld fusion line with a precision cutting device. Each of these samples was then polished, etched, and coated with carbon to obtain carbon extraction replicas. Further, thin foil specimens were prepared by standard polishing procedure followed by jet thinning using an electrolyte of perchloric acid (10 pct) and methanol. In each sample, typical microstructure from five different

Table II. Welding Parameters Used in the Present Study

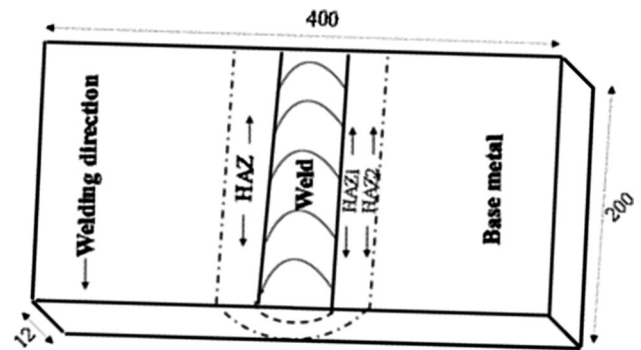| Welding Speed	150 mm/min
Arc gap	1.5 mm
Current	150 A
Voltage	15 V
Gas Flow	10 l/min

Fig. 1—Schematic of the weld geometry (all dimensions in mm).

Table I. Chemical Composition (in Weight Percent) of RAFM Steels Used in the Present Study

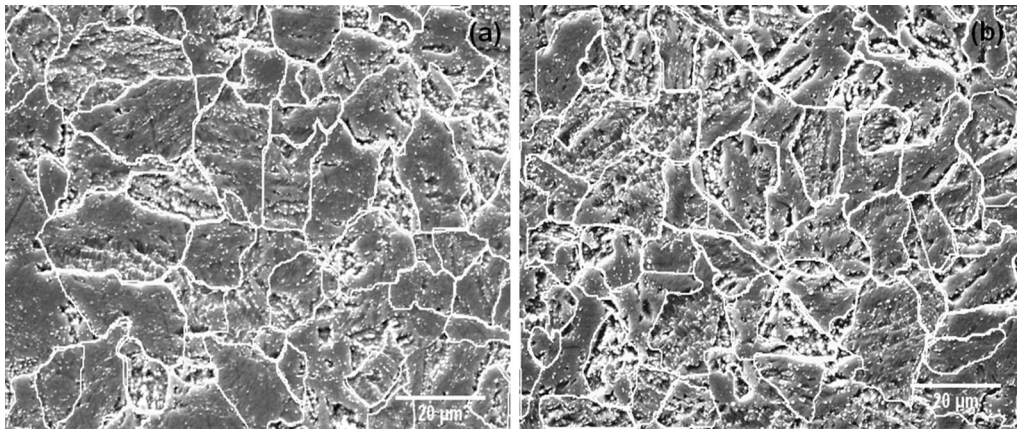| Steel	Cr	C	Mn	V	W	Ta	N	O	Ti	Ni	Mo	Nb
1W	9.04	0.08	0.55	0.22	1.0	0.06	0.02	0.01	0.005	0.005	0.002	0.001
INRAFM	9.03	0.13	0.56	0.24	1.38	0.06	0.03	0.002	0.005	0.005	0.001	0.001

Fig. 2—(a) SEM micrograph of normalized and tempered 1W steel showing prior austenite grains and tempered martensitic structure. (b) SEM micrograph of normalized and tempered INRAFM steel showing prior austenite grains and tempered martensitic structure.
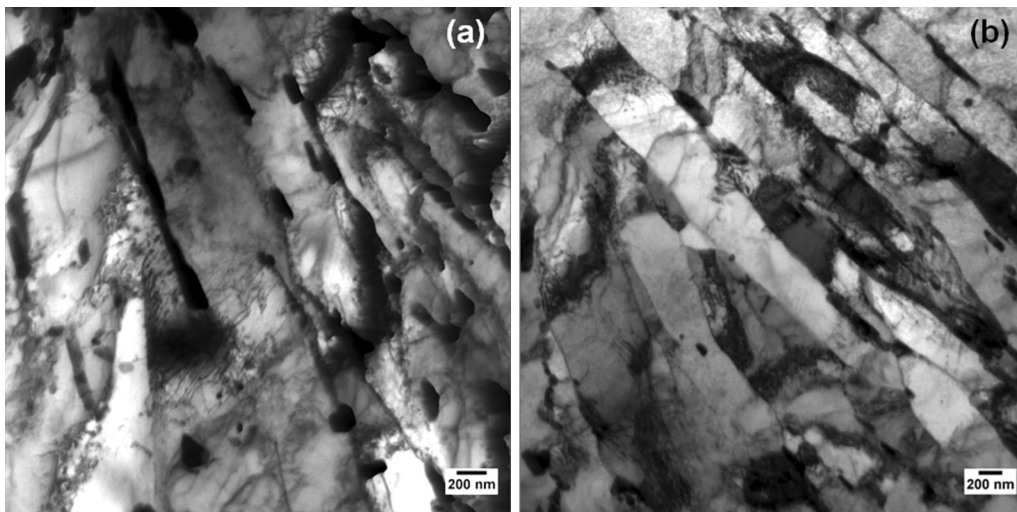

Fig. 3—(a) TEM bright-field image obtained from thin foil of normalized and tempered 1W steel showing lath martensite structure with inter- and intra-lath carbides. (b) TEM bright-field image obtained from thin foil of normalized and tempered INRAFM steel showing lath martensite structure with inter- and intra-lath carbides.

locations were examined to arrive at a conclusion on the type, chemistry, and volume fraction of carbides. A spot size of 15 to 10 nm was used for EDS analysis on carbon extraction replicas. The precipitates were identified by analysis of the selected area diffraction (SAD) and microdiffraction patterns. Due to wide variation in the precipitate size, a frequency distribution plot has been made. Volume fraction of carbides was estimated from TEM micrographs using "Image J" software. Approximately, 4000 to 5000 precipitates were used for image analysis.

JMatPro was used to determine change in phase constitution as a function of composition and temperature. Correctness of the underlying thermodynamic data was checked by comparing the predicted (using JMatPro) phase transformation temperatures with that of experimental calorimetry measurements.[32] In the present study, computation of the phase evolution took into consideration the difference in composition between the RAFM steels and the thermal cycle undergone by

different regions of the weldment during TIG welding.[22] Equilibrium phases were identified by thermodynamic calculations using Gibb's energy minimization routines proposed by Kattner et al.[33] and Lukas et al.[34]

III. RESULTS AND DISCUSSION

A. Identification of Equilibrium Phases in Normalized and Tempered Steels (Base Metal)

The SEM micrographs of 1W and INRAFM steels in the normalized and tempered condition are shown in Figures 2(a) and (b), respectively. As expected, the steels possess a tempered martensitic structure, with an average PAG size of ~14 and 10 μm, respectively. The average hardness is in the range of 220 to 230 VHN. The TEM bright-field images in Figure 3 revealed a high density of dislocations and the lath width measured are in the range of ~500 to 600 nm. Precipitates of various

sizes and morphologies decorated the prior austenite and lath boundaries.

Typical TEM micrograph of carbon extraction replica from INRAFM steel and diffraction patterns obtained from two different types of precipitates are shown in Figure 4(a). Analysis of the microdiffraction patterns confirmed the presence of $M_{23}C_6$ and MX carbides along $\langle \bar{1}14 \rangle$ and $\langle 1\bar{2}1 \rangle$ zone axis, respectively, the former being more predominant. Analysis of the EDS spectra (Figure 4(b)) showed $M_{23}C_6$ to be Cr rich (~58 wt pct) with W content as high as 11 wt pct. However, MX carbides were found to be rich either in V or Ta (Figure 4(c)). In fact, the composition served as a unique signature to distinguish the two types of precipitates. Size distribution of $M_{23}C_6$ carbides

(Figure 4(d)) showed a Gaussian distribution with an average size range of 70 to 100 nm. In contrast, MX carbides were few and of very fine size in the range of 10 to 15 nm. Volume fraction of carbides was higher in INRAFM than in 1W steel owing to the higher concentration of carbon (Table I).

The change in phase fraction as a function of temperature was computed using JMatPro for the two steels and the results of INRAFM steel, is depicted in Figure 5(a). It is seen that Laves and M_2X phases were stable only up to 923 K and 763 K (650 °C and 490 °C,) respectively for the given steel composition. Predicted equilibrium phases in the temperature range of interest [1000 K to 1253 K (727 °C to 980 °C)] were $M_{23}C_6$, MX, ferrite, and austenite. Dissolution temperature of
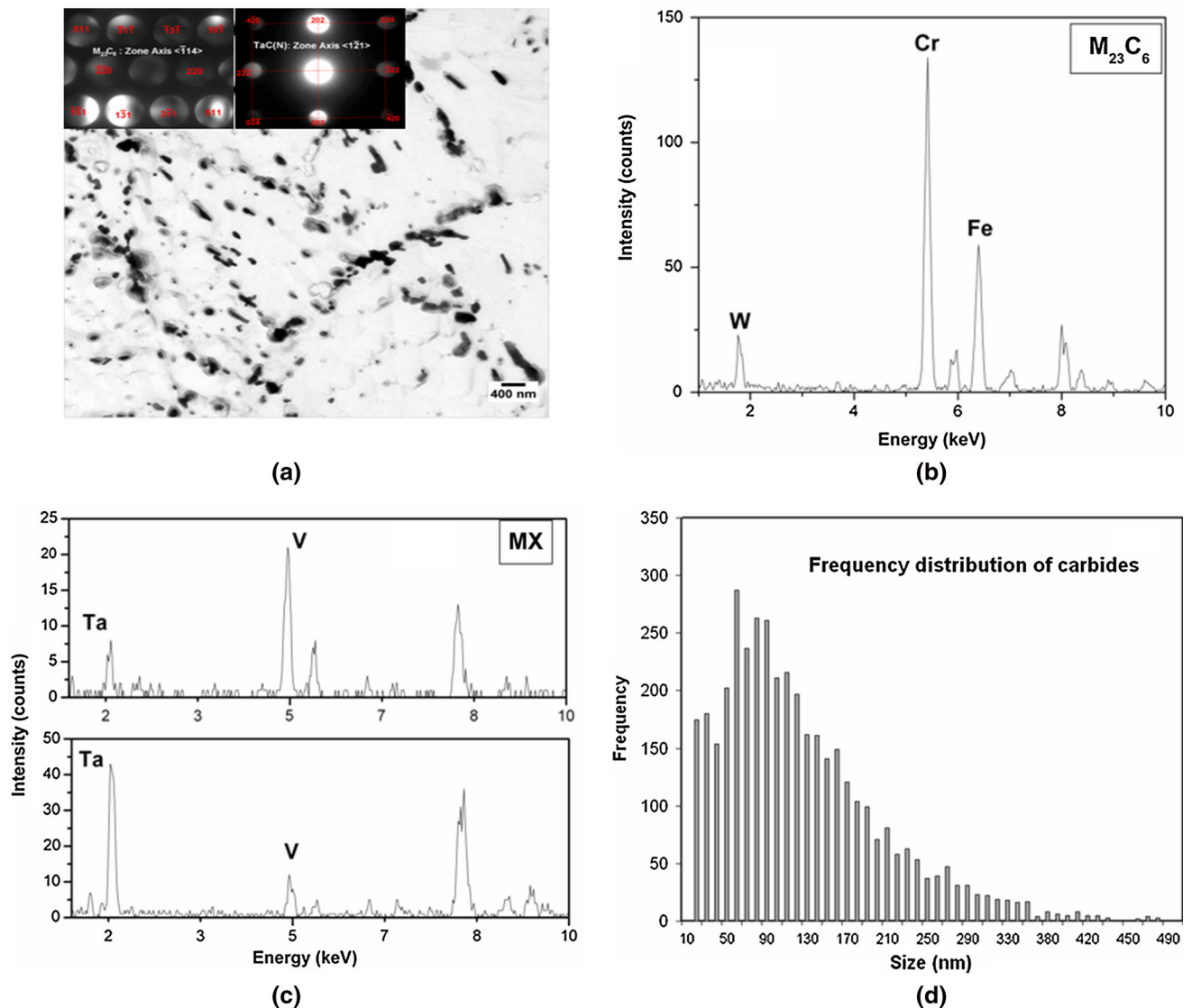

Fig. 4—(a) TEM micrograph and typical micro diffraction patterns of $M_{23}C_6$ and MX carbides obtained from 'as received' INRAFM steel. (b) EDS spectra showing Cr enrichment in $M_{23}C_6$ obtained from 'as received' INRAFM steel. (c) EDS spectra showing V and Ta enrichment in MX carbides obtained from 'as received' INRAFM steel (d) Frequency distribution with respect to the size of $M_{23}C_6$ carbides obtained from 'as received' INRAFM steel.
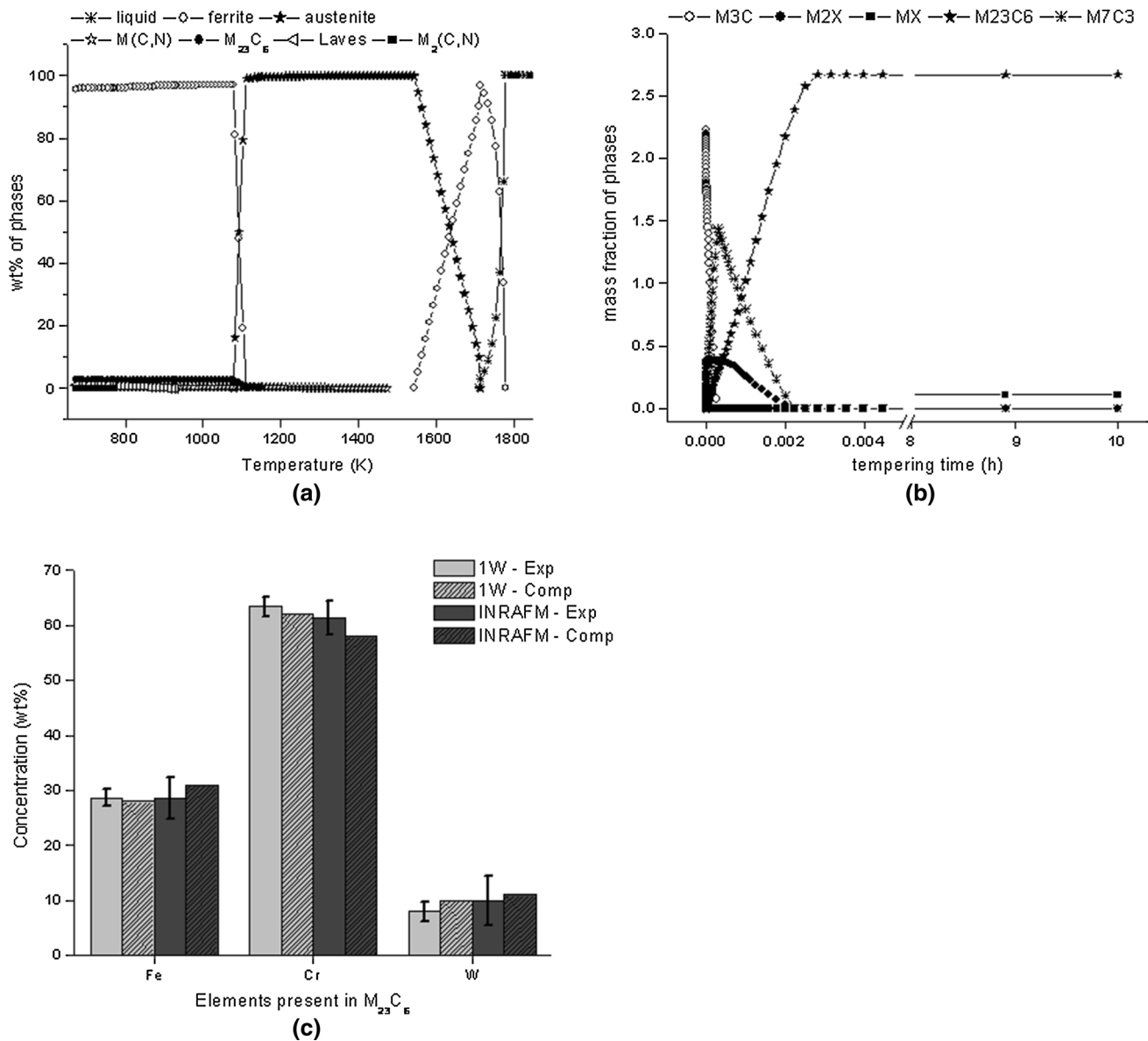
Fig. 5—(a) Plot of distribution of various phases as a function of temperature for INRAFM steel calculated using JMatPro. (b) Change in phase fraction as a function of tempering time at 1033 K (760 °C) for INRAFM steel calculated using JMatPro. (c) Comparison of experimental and computed concentration of $M_{23}C_6$ carbides in both 1W and INRAFM steels.

$M_{23}C_6$ was found to be higher in INRAFM as compared to 1W steel, which was attributed to the higher amount of W in the carbide.[35] Change in phase fraction with time at a temperature of 1033 K (760 °C) for INRAFM steel as computed using JMatPro is given as Figure 5(b). In contrast to normalized and tempered microstructure obtained experimentally, JMatPro-based computations assumed that the alloy was quenched from a temperature above Ac3 followed by tempering at a chosen temperature for specified durations. Effect of pre-existing carbides (due to normalizing) on the availability of carbon in the matrix, competitive dissolution and coarsening of carbides, and change in their microchemistry with heat treatment were not considered. Nevertheless, in agreement with experimental observations (Figure 4) predominantly $M_{23}C_6$ with few MX

carbides were predicted to form after 1h. Computed concentration of major alloying elements *i.e.*, Fe, Cr, and W in $M_{23}C_6$ carbide (both 1W and INRAFM) also agreed with the values obtained by EDS analysis (Figure 5(c)). A similar comparison could not be made for the MX carbide since both Ta- and V-rich MX carbides with wide range of mutual solubility were identified. Likewise computations showed that the expected size of $M_{23}C_6$ and MX carbides were 109 and 8 nm, respectively, after tempering for 1 hour at 1033 K (760 °C), whereas experimentally $M_{23}C_6$ exhibited a unimodal distribution (Figure 4(d)) with a peak size range of 70 to 100 nm and MX size varied between 10 and 20 nm.

Validity of applying JMatPro to RAFM steels was checked again by determining the microchemistry of

precipitates in the base metal. Partitioning of tungsten and tantalum among various phases in INRAFM steel is shown in Figures 6(a) and (b), respectively. The presence of W in both ferrite and $M_{23}C_6$ phases suggested that unlike Cr, it not only acted as ferrite stabilizer but also provided enhanced solid solution strengthening and precipitation hardening. JMatPro correctly predicted the incorporation of W into $M_{23}C_6$ carbide and increased tendency for Laves phase formation in W containing steels as reported in literature.[36] In contrast Ta has a higher affinity for carbon and gets precipitated as carbides (Figure 6(b)) with a maximum of only 2 to 3 wt pct solubility in the ferrite matrix. Below 923 K (650 °C), percentage of Ta present in Laves phase increased with decrease in temperature. Vanadium was predominantly associated with the MX phase with limited solubility in the $M_{23}C_6$ carbide.

B. Microstructural Changes Across the Weldment of RAFM Steels

The weldments of RAFM steel showed a heterogeneous microstructure (Figure 7) with the formation of only martensite in the weld region (WM) and a duplex ($\alpha' + \alpha$) microstructure in the HAZ away from fusion line. The regions designated as HAZ1 (Figure 1) comprised coarse-grained heat-affected zone (CGHAZ), while HAZ2 (Figure 1) consisted of fine-grained heat-affected zone (FGHAZ) and the Inter-Critical heat-affected zone. Complete microstructural and microchemical descriptions of the zones are available elsewhere.[37] No evidence was obtained for the presence of delta ferrite or tantalum oxides in the weld metal, in contrast to reported literature for TIG-welded CLAM steel.[38] The present observations are also supported by the chromium and nickel equivalents[39] for 1W and INRAFM steels evaluated as (11.2, 3.2) and (11.5, 4.8),

respectively. Superimposing these values on Schaffler–Schneider diagram showed that martensite is the only constituent that forms in the WM at ambient temperature following cooling from austenizing temperature.

Hardness profile obtained across the weldment (superimposed in Figure 7) showed the expected trend of high hardness in the WM followed by a continuous decrease across the HAZ until the base metal. This
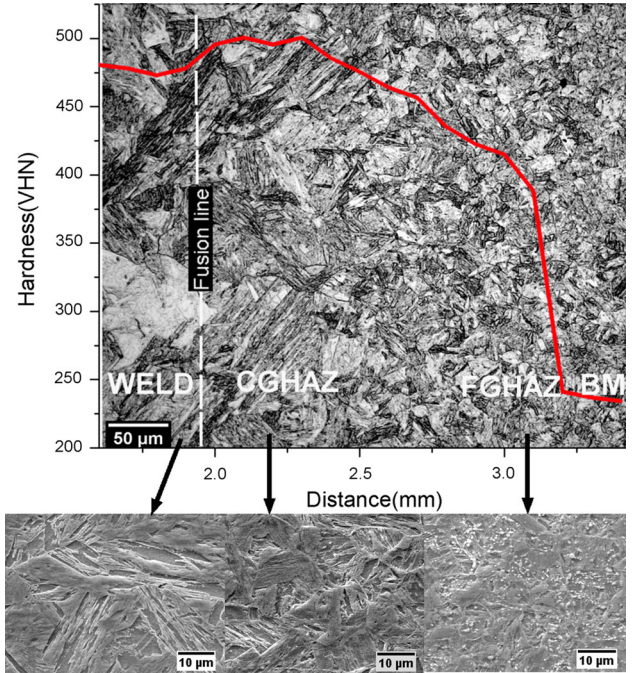
Fig. 7—Optical (top) and SEM micrographs with superimposed hardness profile showing different regions in 1W RAFM steel weldments.
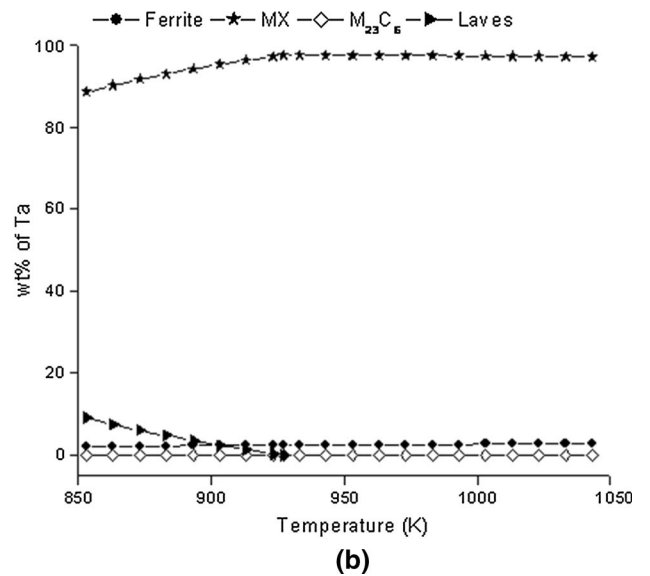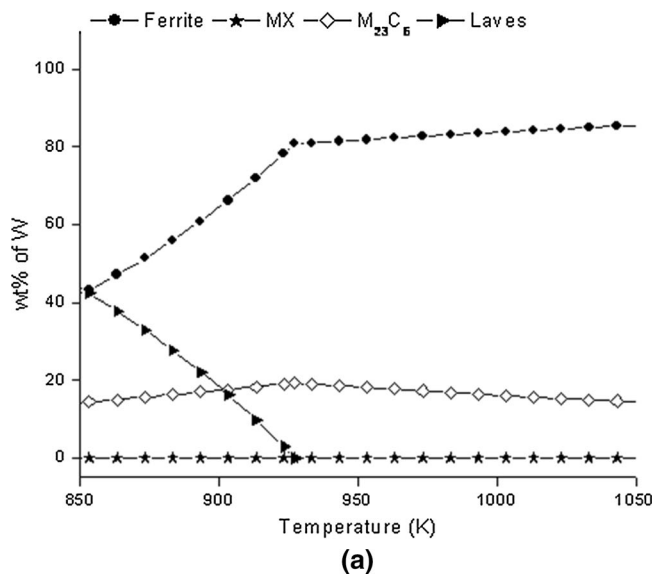
Fig. 6—(a) Plot of distribution of W among various phases as a function of temperature in INRAFM steel as calculated using JMatPro. (b) Plot of distribution of Ta among various phases as a function of temperature in INRAFM steel as calculated using JMatPro.

variation was in agreement with the substructure and decreasing amount of carbon super saturation in martensite, as dictated by the residence time and the peak temperatures witnessed by the respective regions. High hardness of WM and HAZ1 (~530 and 514 VHN) of INRAFM steel as compared to that of 1W steel (~500 and 465 VHN) is attributed to the high solute and carbon contents.

C. Microstructural Evolution Across the Weldment of RAFM Steels Upon Thermal Exposure

The microstructural changes occurring across the weldments of RAFM steels upon aging in the temperature range of 773 K to 873 K (500 °C to 600 °C) have been investigated to obtain insights into the integrity of the weld joint during long-term service exposures. Further, there are reports of embrittlement in the vicinity of 823 K (550 °C) in similar ferritic-martensitic steels.[40,41] Hence, detailed computations using JMatPro was carried out in the temperature range of 773 K to 873 K (500 °C to 600 °C) to investigate the difference in the precipitation sequence of secondary phases, their mole fraction, and coarsening rate between different regions in the weldments of the two steels. Experimental investigations were carried out for selected temperature–time combinations to get confirmatory evidence for validation of the predictions. Results of these studies are presented in the following sections.

1. Thermal exposure-induced microstructural evolution in the base metal

The sequence of evolution of secondary phases in 1W and INRAFM steel as a consequence of thermal aging at 773 K, 823 K, and 873 K (500 °C, 550 °C, and 600 °C) for durations in the range of 1 to 10,000 hours has been computed using JMatPro. The computation predicts the type and volume fraction of the different phases that form as a function of aging time at different temperatures. A summary of the results is listed in Table III. Following are the significant differences observed in INRAFM steel as compared to 1W steel.

- Early onset of precipitation of MX carbides was observed specifically at 823 K and 873 K (550 °C and 600 °C).
- M_2X carbonitrides were stable only up to 4 hours of heat treatment at 873 K (600 °C).
- Although Laves phase formed in both the steels after 1000 hours of aging at 823 K (550 °C), its volume fraction (V_f^{LP}) was relatively higher in INRAFM steel ($V_f^{INRAFM} = 0.003$ vs $V_f^{1W} = 0.001$).
- At 873 K (600 °C) Laves phase formed after 100 hours of aging itself, its volume fraction (V_f^{LP}) predicted to be extremely small (0.001) in comparison to that of $M_{23}C_6$ (2.7) and MX (0.091) carbides.
- After 5000 hours of aging at 873 K (600 °C), Laves phase was the second most predominant phase ($V_f^{LP} = 0.228$) next to $M_{23}C_6$ ($V_f^{M_{23}C_6} = 2.7$).
- For all temperature–time combinations volume fraction of secondary phases was relatively higher.

Table III. Summary of Computational Results Showing Differences in the Precipitation Sequence of Secondary Phases in the Base Metal of 1W and INRAFM Steels After Thermal Aging for Various Durations

| Aging Time (h)	1W RAFM			INRAFM		
	773 K (500 °C)	823 K (550 °C)	873 K (600 °C)	773 K (500 °C)	823 K (550 °C)	873 K (600 °C)
1	M_7C_3, $M_{23}C_6$, M_3C, M_2X	$M_{23}C_6$, M_2X, M_7C_3	$M_{23}C_6$, M_2X	M_7C_3, $M_{23}C_6$, M_3C, M_2X	$M_{23}C_6$, M_2X, M_7C_3	$M_{23}C_6$, M_2X
2	M_7C_3, $M_{23}C_6$, M_2X	$M_{23}C_6$, M_2X	$M_{23}C_6$, M_2X	M_7C_3, $M_{23}C_6$, M_2X	$M_{23}C_6$, M_2X	$M_{23}C_6$, M_2X, MX
10	$M_{23}C_6$, M_2X	$M_{23}C_6$, M_2X	$M_{23}C_6$, MX, M_2X	$M_{23}C_6$, M_2X	$M_{23}C_6$, M_2X, MX	$M_{23}C_6$, MX
100	$M_{23}C_6$, M_2X	$M_{23}C_6$, MX	$M_{23}C_6$, MX	$M_{23}C_6$, M_2X	$M_{23}C_6$, MX	$M_{23}C_6$, MX, Laves
1000	$M_{23}C_6$, MX	$M_{23}C_6$, MX, Laves	$M_{23}C_6$, MX, Laves	$M_{23}C_6$, MX	$M_{23}C_6$, MX, Laves	$M_{23}C_6$, MX, Laves
5000	$M_{23}C_6$, MX	$M_{23}C_6$, MX, Laves	$M_{23}C_6$, MX, Laves	$M_{23}C_6$, MX	$M_{23}C_6$, MX, Laves	$M_{23}C_6$, Laves, MX
10,000	$M_{23}C_6$, MX	$M_{23}C_6$, MX, Laves	$M_{23}C_6$, Laves, MX	$M_{23}C_6$, MX	$M_{23}C_6$, MX, Laves	$M_{23}C_6$, Laves, MX
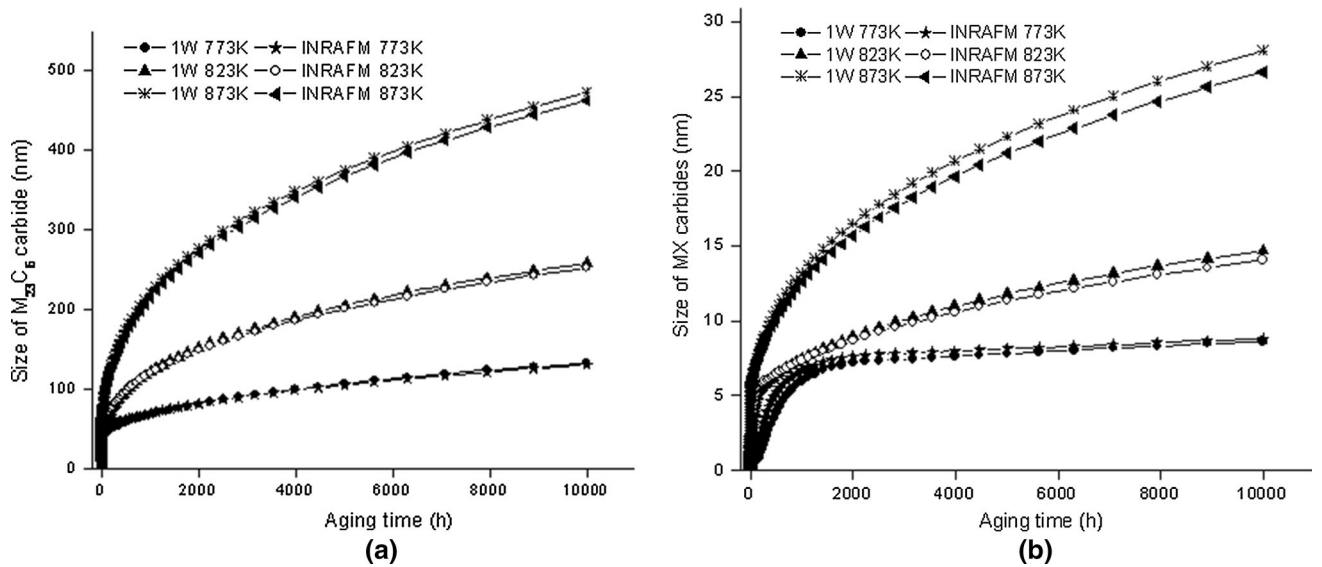
Fig. 8—(*a*) Computed change in the size of $M_{23}C_6$ carbides in the base metal of RAFM steels with aging time for various temperatures. (*b*) Computed change in the size of MX carbides in the base metal of RAFM steels with aging time for various temperatures.

Increase in the volume fraction of carbides and Laves phase in INRAFM steel can be understood in terms of the relatively high concentration of carbon and tungsten. The computed change in the size of $M_{23}C_6$ and MX carbides plotted as a function of aging time for various temperatures is shown in Figures 8(a) and (b), respectively for the two steels. As expected, coarsening rate of MX carbides was found to be much lower than that of $M_{23}C_6$ in both the steels. In addition, average size of the precipitates in INRAFM steel was lower than that in 1W steel.

Although JMatPro-based computations helped in identifying different phases and their stability ranges in the RAFM steels for various temperature–time combinations, precise microstructural details could be obtained only through detailed electron microscopy investigations. Experimental studies were restricted to longer durations of aging (5000 and 10,000 hours) at 773 K and 823 K (500 °C and 550 °C). $M_{23}C_6$ precipitate sizes were estimated from microstructural analysis of a large number of regions and was observed to vary over a wide range of 25 to 500 nm. An analysis of the frequency distribution of precipitates sizes was carried out for all temperature–time combinations in both the steels. It revealed a unimodal Gaussian distribution as depicted in Figure 9 [for INRAFM steel after aging for 10,000 hours at 823 K (550 °C)] and the values quoted are the normalized size of the carbides. The observations described in the following paragraphs hold good for both the steels unless stated otherwise.

Figure 10(a) shows a typical bright-field image of INRAFM steel aged at a temperature of 773 K (500 °C) for 10,000 hours. Coarsening of $M_{23}C_6$ carbides, with a size of ~130 nm was apparent along with recovery of martensite structure with low dislocation density
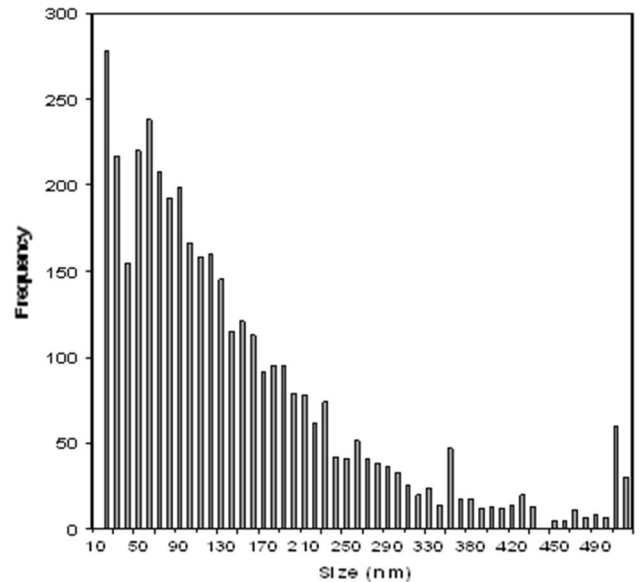

Fig. 9—Frequency distribution with respect to the size of $M_{23}C_6$ carbides obtained from INRAFM steel after aging for 10,000 h at 823 K.

(Figure 10(b)). Inset in Figure 10(b) shows diffraction evidence for the presence of $M_{23}C_6$ carbides along $[1\bar{4}7]$ zone axis. Dark-field image corresponding to $(2\bar{4}2)$ reflection (Figure 10(c)) revealed coarse $M_{23}C_6$ carbides decorating PAG boundary.

Increasing the aging temperature to 823 K (550 °C), showed enhanced rate of recovery as well as coarsening of carbides. Figure 11(a) shows the microstructural details of INRAFM steel after aging for 5000 hours. $M_{23}C_6$ carbides were found to have grown up to an
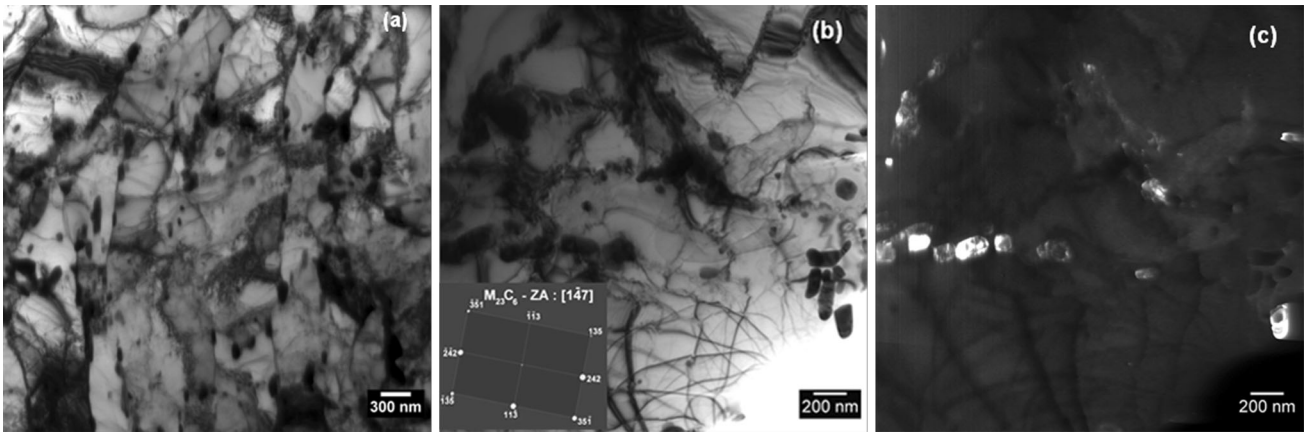
Fig. 10—(a) TEM micrograph of base metal of INRAFM steel aged at 773 K (500 °C) for 10,000 h showing retention of lath structure. (b) TEM micrograph of base metal of INRAFM steel aged at 773 K (500 °C) for 10,000 h showing recovered regions of low dislocation density and carbides (inset shows diffraction pattern from $M_{23}C_6$ carbide along $[1\bar{4}7]$ zone axis). (c) Dark-field image for (2 4 2) reflection highlighting coarse carbides along PAG boundary.
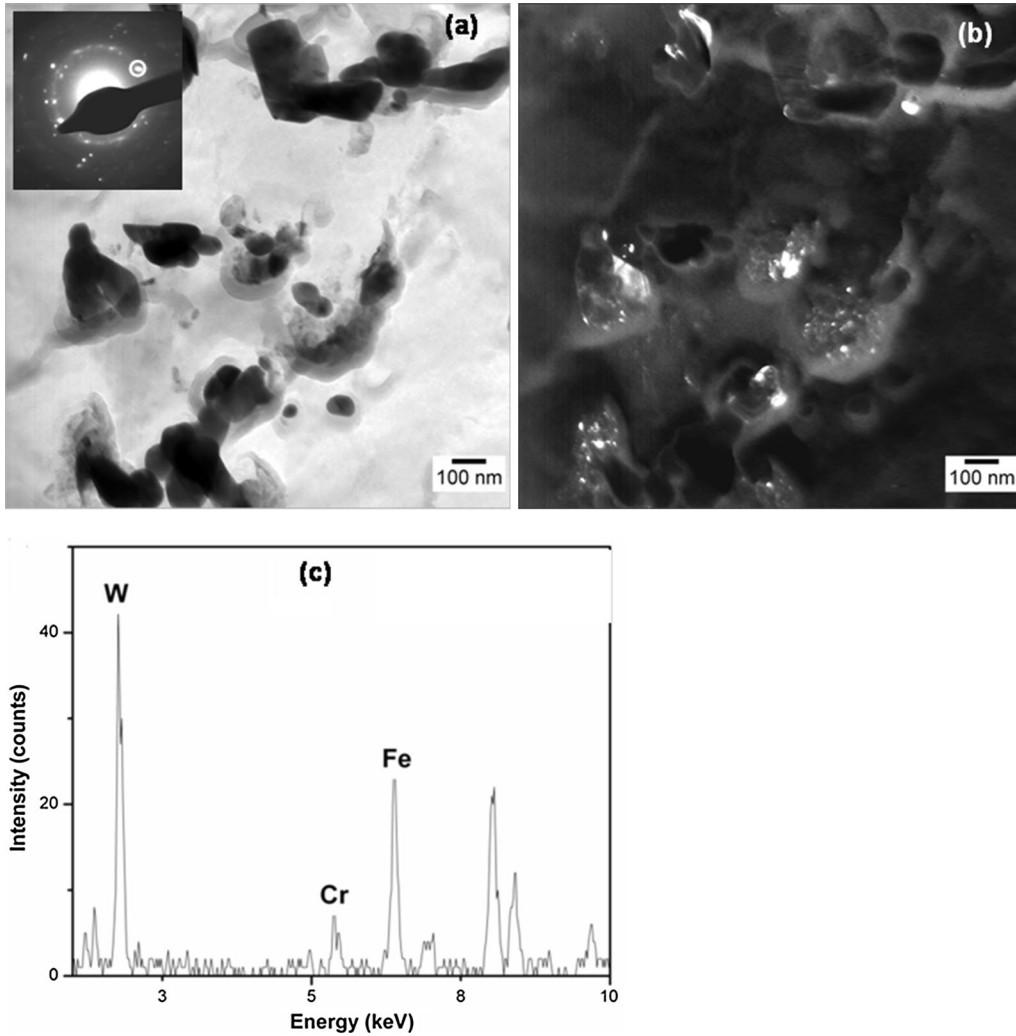

Fig. 11—(a) TEM bright-field image showing carbides along with fine laves phase in the base metal of INRAFM steel after aging at 823 K (550 °C) for 5000 h; inset is the diffraction pattern confirming the presence of laves phase. (b) TEM dark-field image corresponding to circled (001) reflection in (a) showing fine laves phase in the base metal of INRAFM steel after aging at 823 K (550 °C) for 5000 h. (c) EDS spectrum obtained from the base metal of INRAFM steel after aging at 823 K (550 °C) for 5000 h revealing the enrichment of W and Fe in Laves phase.
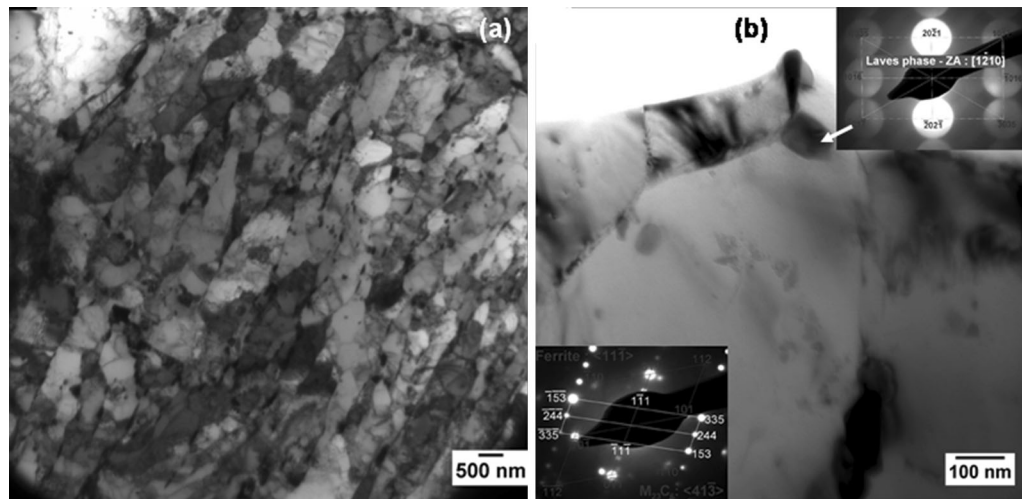
Fig. 12—(*a*) Microstructure of base metal of INRAFM steel after aging at 823 K (550 °C) for 10,000 h showing retention of lath structure. (*b*) Microstructure of base metal of INRAFM steel after aging at 823 K (550 °C) for 10,000 h showing grain boundary carbide and laves phase (arrow marked); insets are the SAD and micro diffraction patterns obtained from M C, carbides and Laves phase along $[41\bar{3}]$ and $[1\bar{2}10]$ zone axis, respectively.

average size of 150 nm. Analysis of the diffraction pattern (inset in Figure 11(a)) identified the presence of an additional 'Laves' phase. TEM dark-field image (Figure 11(b)) corresponding to the circled diffraction spot in Figure 11(a) showed the Laves phase to be very fine (~20 nm) in nature. Typical EDS spectrum (Figure 11(c)) obtained from this fine phase provided clear evidence for the enrichment of W and Fe and hence confirming the formation of Fe_2W-type Laves phase. Laves phase was found to have nucleated around or near the coarse carbides in lath/grain boundaries. Coarsening of carbide consumes large amount of Cr and C, leaving the surrounding matrix depleted in Cr. This results in localized increase in W concentration favoring the nucleation of Laves phase, in the presence of the thermodynamic driving force for its formation. No evidence was obtained for the presence of Laves phase in 1W steel though $M_{23}C_6$ carbides showed similar enrichment for Cr.

With increase in aging time to 10,000 hours, microstructure showed considerable changes. Figures 12(a) and (b) show the TEM micrographs and diffraction pattern obtained from INRAFM steel. Although the lath morphology was retained in several regions (Figure 12(a)) coarser carbides had grown up to an average size of 175 nm and the Cr content in the carbide was ~65 wt pct. In most of the regions Laves phase was observed to grow encapsulating the existing carbides, resulting in an apparent increase in its size. Figure 12(b) shows a region with low dislocation density containing both $M_{23}C_6$ carbide and Laves phase, confirmed based on the analysis of the SAD and microdiffraction patterns (given as inset). Average size of MX phase remained stable at 30 to 40 nm confirming its stipulated contribution to the creep strength of the steel. Even

though JMatPro-based computations indicated the formation of Laves phase in 1W steel (with relatively low V_f) no experimental evidence could be obtained for its presence possibly due to the following reasons: JMatPro predicts only the equilibrium phases that can form for a given alloy composition and does not incorporate the kinetic contribution to phase formation such as (a) enhanced diffusivity of alloying elements in grain/lath boundaries (b) interaction of a diffusing species with other alloying elements (c) effect of grain/lath size variation, and (d) simultaneous dissolution and precipitation of $M_{23}C_6$ carbides leading to local concentration fluctuations in its vicinity, which may promote the formation of Laves phase.

2. Thermal exposure-induced microstructural evolution in the weld metal

Summary of computational results showing differences in the precipitation sequence of secondary phases in the weld metal of 1W and INRAFM steels after thermal aging for various durations is shown in Table IV. Following are the important inferences drawn in comparison with the base metal:

- Volume fraction of all phases was lower.
- Formation of MX carbides was not preferred except at high temperature [873 K (600 °C)] beyond 1000 hours of heat treatment.
- M_3C carbides formed only in INRAFM steel for 1 hour of exposure at 773 K (500 °C)
- Laves phase precipitation was delayed in both the steels. Time required for its precipitation in INRAFM steel was found to be ≥5000 hours at 823 K (550 °C) and ≥1000 hours at 873 K (600 °C). For the same

Table IV. Summary of Computational Results Showing Differences in the Precipitation Sequence of Secondary Phases in the Weld Metal of 1W and INRAFM Steels After Thermal Aging for Various Durations

	1W RAFM			INRAFM		
Aging Time (h)	773 K (500 °C)	823 K (550 °C)	873 K (600 °C)	773 K (500 °C)	823 K (550 °C)	873 K (600 °C)
1	M_7C_3, $M_{23}C_6$, M_2X	$M_{23}C_6$, M_2X	$M_{23}C_6$, M_2X	M_7C_3, $M_{23}C_6$, M_2X, M_3C	$M_{23}C_6$, M_2X, M_7C_3	$M_{23}C_6$, M_2X
2	M_7C_3, $M_{23}C_6$, M_2X	$M_{23}C_6$, M_2X	$M_{23}C_6$, M_2X	M_7C_3, M_2X, $M_{23}C_6$	$M_{23}C_6$, M_2X	$M_{23}C_6$, M_2X
10	$M_{23}C_6$, M_2X	$M_{23}C_6$, M_2X	$M_{23}C_6$, M_2X	M_7C_3, M_2X, $M_{23}C_6$	$M_{23}C_6$, M_2X	$M_{23}C_6$, M_2X
100	$M_{23}C_6$, M_2X	$M_{23}C_6$, M_2X	$M_{23}C_6$, M_2X	M_7C_3, M_2X, $M_{23}C_6$	$M_{23}C_6$, M_2X	$M_{23}C_6$, MX, M_2X
1000	$M_{23}C_6$, M_2X	$M_{23}C_6$, M_2X	$M_{23}C_6$, M_2X, MX	$M_{23}C_6$, M_2X, M_7C_3	$M_{23}C_6$, M_2X	$M_{23}C_6$, Laves, MX, M_2X
5000	$M_{23}C_6$, M_2X	$M_{23}C_6$, M_2X, Laves	$M_{23}C_6$, Laves, M_2X, MX	$M_{23}C_6$, M_7C_3, M_2X	$M_{23}C_6$, Laves, M_2X	$M_{23}C_6$, Laves, MX, M_2X
10,000	$M_{23}C_6$, M_2X	$M_{23}C_6$, Laves, M_2X	$M_{23}C_6$, Laves, M_2X, MX	$M_{23}C_6$, M_7C_3, M_2X	$M_{23}C_6$, Laves, M_2X	$M_{23}C_6$, Laves, MX, M_2X

temperature–time combination laves phase volume fraction was relatively high in INRAFM steel.

Microstructural details of weld metal of INRAFM steel after aging at 773 K (500 °C) for 5000 hours and 823 K (550 °C) for 10,000 hours are shown as Figure 13(a through c), respectively. Weld metal aged at lower temperature [773 K (500 °C)] consisted of two types $M_{23}C_6$ carbides which could be distinguished in terms of their Cr contents and morphology. Extremely fine (10 to 15 nm) carbides (circled in Figure 13(a)) which were aligned in two perpendicular directions had higher Cr contents (~80 wt pct) when compared to the coarse carbides (~60 to 65 wt pct). These type of carbides maintained their morphology, size, and microchemistry even after 10,000 hours of aging. Other type of carbides indexed as $M_{23}C_6$ were present in sizes ranging from 25 to 420 nm with the peaking of the frequency distribution seen around 50 nm. Cr concentration of these carbides was lower than those observed in the base metal.

It is known in literature[20,42] that Fe-rich $M_{23}C_6$, ε carbides and Cr-rich Cr_2C hexagonal carbides form during the early stages of tempering (or low temperature exposure) of martensitic steels. They subsequently get transformed to Cr-rich $M_{23}C_6$ with progress in tempering. No evidence for MX carbides was observed in the aged steel for the same reason. Nucleation of Laves phase in the weld region on aging at 823 K (550 °C) was observed after 10,000 hours. This delay as compared to the base metal arises from the initial carbide-free martensite structure in the weld and the slow consumption of carbon as tempering/aging proceeds at temperatures lower than the optimum tempering temperature. The weld region of 1W steel showed no evidence for the presence of Laves phase in contrast to JMatPro results the reason for which is the same as that explained earlier in Section III–C–1.

3. Microstructural evolution in the HAZ

Table V presents the summary of computational results corresponding to the FGHAZ of 1W and INRAFM steels after thermal aging for various durations. Similar computations carried out for CGHAZ showed analogous behavior as that of the weld metal. Precipitation sequence, volume fraction, and size of the secondary phases in FGHAZ was similar to that of the base metal (refer Table III). However, an important observation was the relatively early onset of precipitation of Laves phase in both 1W and INRAFM steels on aging at a lower temperature of 773 K (500 °C) itself.

Experimental investigations carried out using electron microscopy revealed high volume fraction of $M_{23}C_6$ carbides in HAZ compared to other regions of the weldment. Coarsening of carbide was found to be highest (350 to 400 nm) in FGHAZ after heat treatment at a temperature of 823 K (550 °C) for 10,000 hours. The observed precipitation and coarsening of carbides revealed by experimental studies and not through computations is a clear manifestation of the effect of prior microstructure (grain/lath sizes) on the kinetics of precipitation. This effect is not reflected in the computations since it incorporates only alloy composition and
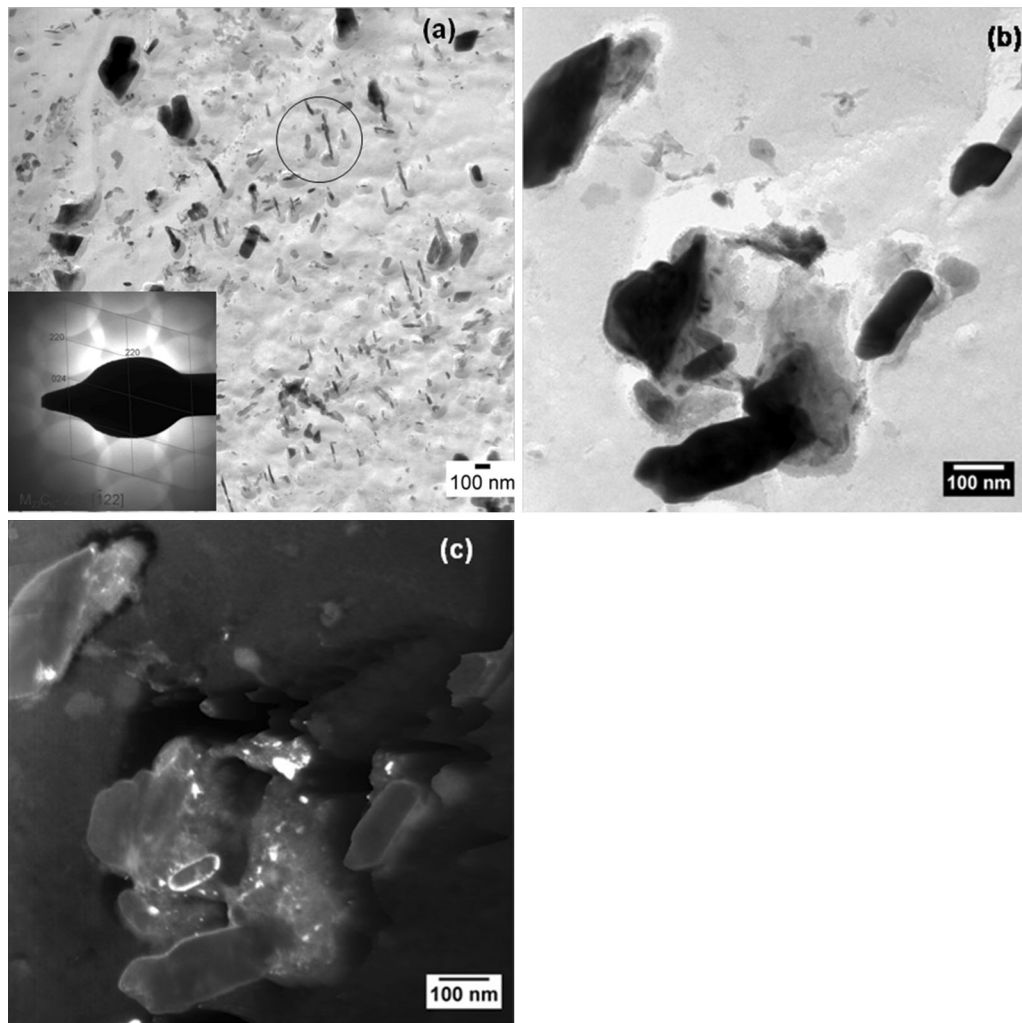
Fig. 13—(*a*) Microstructure of weld metal in INRAFM steel after aging at 773 K (500 °C) for 5000 h showing the presence of fine needle shaped carbides. (*b*) Microstructure of weld metal of INRAFM steel showing the presence of coarse $M_{23}C_6$ carbides after aging at 823 K (550 °C) for 10,000 h (*c*) Dark-field image for (112) reflection highlighting the laves phase surrounding the coarse carbide after aging the weld metal of INRAFM steel at 823 K for 10,000 h.

temperature as input parameters. Figures 14(a) and (b) show the morphology of Laves phase in the FGHAZ of INRAFM steel after aging at 823 K (550 °C) for 5000 and 10,000 hours, respectively. Laves phase at 5000 hours was fine with an average size of 40 nm, whereas it was grown up to ~100 nm after 10,000 hours of aging. In comparison to the base metal, Laves phase was coarser in FGHAZ which suggested that it might have formed first in the FGHAZ of the weldment. Precipitation of Laves phase has been reported earlier in the HAZ of F82H (8Cr-2WVTa) steel after thermal aging at 823 K (550 °C) for 3000 hours.[43]

The evolution of various phases in the three regions of 1W and INRAFM steel weldments after prolonged service exposures for 10,000 hours is consolidated as a schematic in Figures 15(a) and (b), respectively. Com-

pared to 1W steel formation of Laves phase occurred early in INRAFM steel due to higher W content and abundant precipitation of carbides that increased the availability of W and reduced the supersaturation of carbon in nearby regions.

Based on the experimental and simulation studies it can be summarized that thermal aging of the RAFM weldments (during service exposures) will lead to the formation of Laves phase and coarsening of carbides mainly in the HAZ and base metal regions. Such microstructural modifications are known to be detrimental to the fracture toughness and creep strength of the weldments.[19,21] The thermal cycle during welding experienced by the HAZ, favors extensive nucleation followed by the growth of a discontinuous carbide network especially along the lath boundaries during

Table V. Summary of Computational Results Showing Differences in the Precipitation Sequence of Secondary Phases in the FGHAZ of 1W and INRAFM Steels After Thermal Aging for Various Durations

Aging Time (h)	1W RAFM			INRAFM		
	773 K (500 °C)	823 K (550 °C)	873 K (600 °C)	773 K (500 °C)	823 K (550 °C)	873 K (600 °C)
1	M_7C_3, $M_{23}C_6$, M_3C, M_2X	$M_{23}C_6$, M_2X, M_7C_3	$M_{23}C_6$, M_2X	M_7C_3, M_3C, $M_{23}C_6$, M_2X	$M_{23}C_6$, M_2X	$M_{23}C_6$, M_2X
2	M_7C_3, $M_{23}C_6$, M_2X	$M_{23}C_6$, M_2X, M_7C_3	$M_{23}C_6$, M_2X	M_7C_3, $M_{23}C_6$, M_2X	$M_{23}C_6$, M_2X	$M_{23}C_6$, M_2X, MX
10	$M_{23}C_6$, M_2X	$M_{23}C_6$, M_2X	$M_{23}C_6$, M_2X, MX	$M_{23}C_6$, M_2X	$M_{23}C_6$, M_2X, MX	$M_{23}C_6$, MX
100	$M_{23}C_6$, M_2X	$M_{23}C_6$, MX	$M_{23}C_6$, MX	$M_{23}C_6$, M_2X, MX	$M_{23}C_6$, MX	$M_{23}C_6$, MX, Laves
1000	$M_{23}C_6$, MX	$M_{23}C_6$, MX, Laves	$M_{23}C_6$, MX, Laves	$M_{23}C_6$, MX	$M_{23}C_6$, MX, Laves	$M_{23}C_6$, MX, Laves
5000	$M_{23}C_6$, MX	$M_{23}C_6$, MX, Laves	$M_{23}C_6$, MX Laves,	$M_{23}C_6$, MX, Laves	$M_{23}C_6$, MX, Laves	$M_{23}C_6$, Laves, MX
10,000	$M_{23}C_6$, MX, Laves	$M_{23}C_6$, MX Laves	$M_{23}C_6$, Laves, MX	$M_{23}C_6$, MX, Laves	$M_{23}C_6$, MX, Laves	$M_{23}C_6$, Laves, MX

service exposures. This condition set off the formation of Laves phase in the vicinity of the carbides. The preponderance of Laves phase in HAZ in comparison to base metal and weld metal clearly indicates that it is due to kinetic factors. Based on the size and kinetics of precipitation of deleterious phases, FGHAZ was identified to be the weakest region in the weldment for thermal exposures ≥823 K (550 °C). This observation was in accordance with the reported creep failures in RAFM steel welds.[25]

Our studies have established that initial microstructure and the alloy content plays a significant role in the microstructural evolution in RAFM steels. Despite the Laves phase formation and its effect on creep properties, the INRAFM steel provides an excellent combination of strength and toughness at temperatures not exceeding 773 K (500 °C).

IV. CONCLUSIONS

The microstructural modifications as a function of distance from the fusion line in weldments of 1W-RAFM and INRAFM steels after welding and during thermal exposures were studied by experimental and computational methods. Following are the important conclusions drawn based on the above studies:

1. $M(Cr,Fe,W)_{23}C_6$ and $M(Ta,V)X$ carbides were the predominant precipitate phases in normalized and tempered RAFM steels, their volume fraction relatively higher in INRAFM steel [$V_f^{M_{23}C_6}$ = 2.7 and V_f^{MX} = 0.091 after aging at 873 K (600 °C) for 100 hours]. Coarsening rate of $M_{23}C_6$ carbides was much higher than that of MX.
2. JMatPro-based computations helped in identifying the temperature–time window for the formation of undesirable phases in various regions of RAFM steel weldments. In the base metal of INRAFM steel prolonged aging beyond 5000 hours at 873 K (600 °C) promoted the formation of Laves phase as the second most predominant phase after $M_{23}C_6$.
3. Experiments carried out for few selected temperature–time combinations confirmed the formation of Fe_2W-type Laves phase in both FGHAZ and base metal of INRAFM steel after prolonged exposure to temperatures ≥823 K (550 °C). Although JMatPro predicted the formation of Laves phase in 1W-RAFM steel, experiments revealed that they are not kinetically favored.
4. Enhanced precipitation of Laves phase observed in the FGHAZ of INRAFM steel weldments was attributed to the abundance of carbides in this region resulting in a decreased availability of carbon and the higher concentration of W.
5. Due to enhanced kinetics of precipitation of Laves phases, FGHAZ was identified to be the region susceptible for failure during long-term service exposures of INRAFM steel weldments.
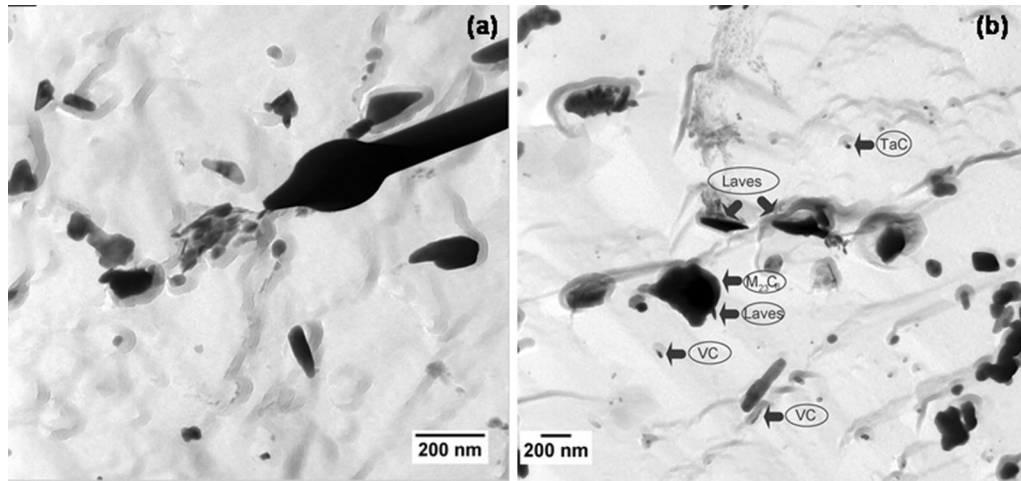
Fig. 14—(*a*) TEM micrographs of carbon extraction replicas from FGHAZ of INRAFM steel aged at 823 K (550 °C) showing fine precipitates of laves phase after 5000 h of heat treatment. (*b*) TEM micrographs of carbon extraction replicas from FGHAZ of INRAFM steel aged at 823 K (550 °C) showing coarse laves phase after 10,000 h of heat treatment.
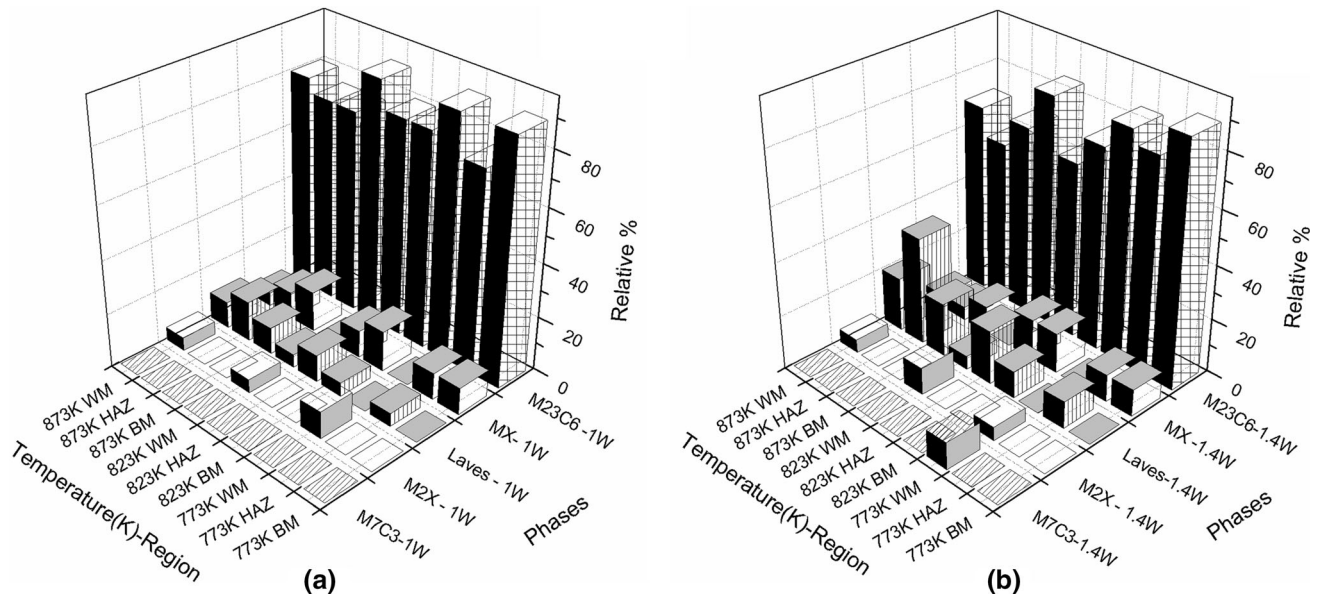

Fig. 15—(*a*) Schematic showing relative amount of various phases present in the different regions of 1W RAFM steel weldment after aging at 773 K to 873 K (500 °C to 600 °C) for 10,000 h. (*b*) Schematic showing relative amount of various phases present in the different regions of INRAFM steel weldment after aging at 773 K to 873 K (500 °C to 600 °C) for 10,000 h.

REFERENCES

1. B. Raj and T. Jayakumar: *J. Nucl. Mater.*, 2011, vol. 417 (1–3), pp. 72–76.
2. R.L. Klueh and E.E. Bloom: *Nucl. Eng. Des./Fusion*, 1985, vol. 2, pp. 383–89.
3. R. Lindau and M. Schirra: *Fusion Eng. Des.*, 2001, vols. 58–59, pp. 781–85.
4. A. Alamo, J.C. Brachet, A. Castaing, C. Lepoittevin, and F. Barcelo: *J. Nucl. Mater.*, 1998, vols. 258–263, pp. 1228–35.
5. B. Van der Schaaf, F. Tavassoli, C. Fazio, E. Rigal, E. Diegele, R. Lindau, and G. LeMorois: *Fusion Eng. Des.*, 2003, vol. 69, pp. 197–203.
6. J.F. Salavy, L.V. Boccaccini, P. Chaudhuri, S. Cho, M. Enoeda, L.M. Giancarli, R.J. Kurtz, T.Y. Luo, K. Bhanu Sankara Rao, and C.P.C. Wong: *Fusion Eng. Des.*, 2010, vol. 85, pp. 1896–1902.
7. M. Tamura, H. Hayakawa, A. Yoshitake, A. Hishinuma, and T. Kondo: *J. Nucl. Mater.*, 1988, vols. 155–157, pp. 620–25.
8. R.L. Klueh: *Int. Mater. Rev.*, 2005, vol. 50 (5), pp. 287–310.
9. F. Abe, T. Noda, H. Araki, and S. Nakazawa: *J. Nucl. Mater.*, 1991, vols. 179–181, pp. 663–66.
10. R.L. Klueh, D.J. Alexander, and M.A. Sokolov: *J. Nucl. Mater.*, 2002, vol. 304, pp. 139–52.

11. L. Schaefer and M. Schirra: *J. Nucl. Mater.*, 1999, vols. 271–272, pp. 455–58.
12. Y. Wei, W. Wei, S. Yi-Yin, and Y. Ke: *Front. Mater. Sci.*, 2013, vol. 7 (1), pp. 1–27.
13. S. Ghosh: *J. Mater. Sci.*, 2010, vol. 45, pp. 1823–29.
14. R.L. Klueh, N. Hashimoto, and M.A. Sokolov: *ASTM Spec. Tech. Publ.*, 2004, vol. 1447, pp. 376–90.
15. T. Hasegawa, Y. Tomita, and A. Kohyama: *J. Nucl. Mater.*, 1998, vols. 258–263, pp. 1153–57.
16. P. Aubert, F. Tavassoli, M. Reith, and Y. Poitevin: *J. Nucl. Mater.*, 2011, vol. 417, pp. 43–50.
17. A. Alamo, A. Castaing, A. Fontes, and P. Wident: *J. Nucl. Mater.*, 2000, vols. 283–287, pp. 1192–95.
18. H. Hayakawa, A. Yoshitake, M. Tamura, S. Natsume, A. Gotoh, and A. Hishinuma: *J. Nucl. Mater.*, 1991, vols. 179–181, pp. 693–96.
19. D. Young Ku, S. Oh, M.-Y. Ahn, I.-K. Yu, D.-H. Kim, S. Cho, I.-S. Choi, and K.-B. Kwon: *J. Nucl. Mater.*, 2011, vol. 417 (1), pp. 67–71.
20. Z. Jiang, L. Ren, J. Huang, X. Ju, H. Wu, Q. Huang, and Y. Wu: *Fusion Eng. Des.*, 2010, vol. 85, pp. 1903–908.
21. M. Vijayalakshmi, S. Saroja, V. Thomas Paul, R. Mythili, and V.S. Raghunathan: *Metall. Mater. Trans. A*, 1999, vol. 30A, pp. 161–74.
22. V. Thomas Paul, S. Saroja, P. Hariharan, A. Rajadurai, and M. Vijayalakshmi: *J. Mater. Sci.*, 2007, vol. 42, pp. 700–13.
23. D.J. Allen and S.J. Brett: *Proc. International Symposium on Case Histories on Integrity and Failures in Industry*, Milan, Italy, 1999, p. 133.
24. J.A. Francis, W. Mazur, and H.K.D.H. Bhadeshia: *Mater. Sci. Technol.*, 2006, vol. 22 (12), pp. 1387–95.
25. S. Zheng, Q. Wu, Q. Haung, S. Liu, and Y. Han: *Fusion Eng. Des.*, 2011, vol. 86, pp. 2616–19.
26. B. Arivazhagan, G. Srinivasan, S.K. Albert, and A.K. Bhaduri: *Fusion Eng. Des.*, 2011, vol. 86, pp. 192–97.
27. Q. Lu, W. Xu, and S. van der Zwaag: *Metall. Mater. Trans. A*, 2014, vol. 45A, pp. 6067–74.
28. R. Foret, B. Zlamal, and J. Sopousek: *Welding J.*, 2006, vol. 85, pp. 211s–17s.
29. L. Kaufman: *Computer Calculation of Phase Diagrams*, Academic Press, NewYork, 1970.
30. N. Saunders, X. Li, P. Miodownik, and J. Ph. Schille: in *Proc. Symp. Mater. Des. Approaches Exper.*, 2001, pp. 185–97.
31. R.L. Klueh: *J. Nucl. Mater.*, 2008, vol. 378, pp. 159–66.
32. Ravi Kirana, S. Raju, R. Mythili, S. Saroja, T. Jayakumar, and E. Rajendra Kumar: *Steel Res. Inter.*, 2015, DOI: 10.1002/srin.201400183.
33. U.R. Kattner: *JOM*, 1997, vol. 49 (12), pp. 14–19.
34. H.L. Lucas, J. Weiss, and E.Th. Henig: *CALPHAD*, 1982, vol. 6, pp. 229–51.
35. S.G. Hong, W.B. Lee, and C.G. Park: *J. Nucl. Mater.*, 2001, vol. 288, pp. 202–207.
36. J. Hald: *Mater. Technol.*, 1996, vol. 67 (9), pp. 369–74.
37. V. Thomas Paul, S. Saroja, S.K. Albert, T. Jayakamar, and E. Rajendra Kumar: *Mater. Charat.*, 2014, vol. 96, pp. 213–24.
38. Q. Zhu, Y.C. Lei, X.Z. Chen, W.J. Ren, X. Ju, and Y.M. Ye: *Fusion Eng. Des.*, 2011, vol. 86, pp. 407–411.
39. R.L. Klueh and D.R. Harries: *High-Chromium Ferritic and Martensitic Steels for Nuclear Applications,* ASTM MON03, 2001.
40. D.J. Alexander, P.J. Maziasz, and C.R. Brinkman: *Microstructures and Mechanical Properties of Aging Material*, Warrendale, PA, 1993, pp. 343–348.
41. H. Okamura, R. Ohtani, K. Saito, K. Kimura, R. Ishii, K. Fujiyama, S. Hongo, T. Iseki, and H. Uchida: *Nucl. Eng. Des.*, 1999, vol. 193, pp. 243–54.
42. G. Chakraborty, C.R. Das, S.K. Albert, A.K. Bhaduri, V. Thomas Paul, G. Panneerselvam, and A. Dasgupta: *Mater. Charat.*, 2014, vol. 100, pp. 81–87.
43. T. Sawai, K. Shiba, and A. Hishinuma: *J. Nucl. Mater.*, 2000, vols. 283–287, pp. 657–61.